

A workflow for 3D reconstruction and quantification of the monkey optic nerve head vascular network

Po-Yi Lee,^{1,2} Yi Hua,² Bryn L. Brazile,² Bin Yang,^{2,3} Lin Wang,⁴ Ian A. Sigal^{1,2†}

¹ Department of Bioengineering, Swanson School of Engineering

² Department of Ophthalmology, School of Medicine
University of Pittsburgh, Pittsburgh, PA

³ Department of Engineering, Rangos School of Health Sciences
Duquesne University, Pittsburgh, PA

⁴ Devers Eye Institute, Portland, OR

Short title: 3D vascular network reconstruction

† Correspondence:

Ian A. Sigal, Ph.D.

Laboratory of Ocular Biomechanics

Department of Ophthalmology, University of Pittsburgh School of Medicine

203 Lothrop Street, Eye and Ear Institute, Rm. 930, Pittsburgh, PA 15213

Phone: (412) 864-2220; Fax: (412) 647-5880

Email: ian@OcularBiomechanics.com

www.OcularBiomechanics.com

Keywords: Optic nerve head, vasculature, tortuosity, perfusion, fluorescence

Disclosures: Bryn L. Brazile was at the University of Pittsburgh when he contributed to this work. He is now at Baxter; Other authors have nothing to disclose.

Funding: Supported in part by National Institutes of Health R01-EY023966, R01-EY028662, R01-EY031708, R01-HD045590, R01-HD083383, P30-EY008098 and T32-EY017271 (Bethesda, MD), the Eye and Ear Foundation (Pittsburgh, PA), and Research to prevent blindness.

For submission to ASME Journal of Biomechanical Engineering

1 **Abstract**

2 A comprehensive characterization of the 3D vascular network of the optic nerve head (ONH) is
3 critical to understanding eye physiology and pathology. Current in vivo imaging technologies,
4 however, do not have simultaneous high spatial resolution and imaging depth to resolve the small
5 vessels deep within the ONH. We describe a workflow for the 3D reconstruction and quantitative
6 morphological analysis of the ONH vasculature. The vessels of a normal monkey ONH were
7 perfusion labeled. Serial cryosections of the ONH were imaged using fluorescence microscopy
8 (FM) and instant polarized light microscopy (IPOL) to visualize the labeled vessels and label-free
9 collagen, respectively. The IPOL images were registered and used to form a stack of FM images
10 from which the vessels were segmented and skeletonized to reconstruct the 3D vascular network.
11 The network consisted of 12,966 vessel segments, 7,989 branching points, and 1,100 terminal
12 points at the boundaries. For each vessel segment, we measured its length, tortuosity, inclination
13 (θ), and polar orientation (φ). The length followed a lognormal distribution, whereas the
14 distribution of the tortuosity followed an exponential decay. The vessels were mainly oriented
15 towards the coronal plane ($\theta = 90^\circ$). For orientation, there were nearly as many vessels aligned
16 circumferentially ($\varphi = 90^\circ$) and radially ($\varphi = 0^\circ$). Our results demonstrate the workflow for 3D eye-
17 specific reconstruction and quantification of the monkey ONH vascular network. This is a critical
18 first step to analyze the blood flow and oxygenation within the ONH, which will help understand
19 the role of vascular dysfunction in glaucoma.

20 1. Introduction

21 Glaucoma is a leading cause of blindness worldwide [1]. It is characterized by irreversible damage
22 to the retinal ganglion cell axons within the optic nerve head (ONH), specifically within the lamina
23 cribrosa (**Figure 1**). The blood vessels of the ONH form a complex network intertwined with the
24 collagen beams in the lamina cribrosa [2, 3]. The primary risk factor for axon damage is an
25 elevated intraocular pressure [4-10]. However, the level of intraocular pressure that causes axon
26 damage varies substantially between people, with a large number of patients suffering axon loss
27 at apparently normal levels of intraocular pressure [9, 10]. The evidence thus indicates that there
28 are other factors contributing to axon loss and vision loss in glaucoma. It has long been believed
29 that axon damage could also result from an insufficient oxygen supply within the ONH due to
30 compromised blood flow [11-15].

31 To understand the hemodynamic environment within the ONH and the potential role of blood
32 flow and the oxygen supply, a critical first step is to visualize and characterize its 3D vascular
33 network. The vessels of the ONH can be fairly small – 10 to 20 μm in diameter, and deep – several
34 hundred micrometers from the optic disk surface [2, 15]. In addition, some of the vessels are
35 enclosed within collagen beams [2, 16]. Current tools for visualizing posterior pole vasculature in
36 vivo do not have sufficient resolution or imaging depth [16]. For example, optical coherence
37 tomography angiography has a high spatial resolution and provides excellent data on the retina
38 and in some small regions of the LC [17-19]. However, it does not have sufficient imaging depth
39 to visualize the vessels deep inside the ONH. Ultrasound and magnetic resonance imaging have
40 a high imaging depth, but do not have the spatial resolution necessary to discern the small vessels
41 of the ONH [20-27]. Because of the importance of characterizing the ONH vasculature, there have
42 been many attempts to do that ex vivo. One of the most successful was the use of vascular
43 castings, often made in plastic [28, 29]. Analysis of the vascular casts, however, required
44 destroying the rest of the tissues using corrosion methods, which precludes precisely identifying
45 the location of vessels relative to known non-vessel components, such as the collagen. Given the
46 limitations of in vivo imaging and plastic casts, histological imaging remains a powerful alternative
47 to visualize the vessels of the ONH. It allows for a high spatial resolution imaging, and the depth
48 of study is only a matter of studying enough sections.

49 Our goal was to develop a histological imaging workflow allowing reconstruction and
50 quantitative morphological analysis of the full 3D vascular network of the ONH. The workflow
51 should allow visualization of non-vascular tissues for context, and the reconstruction and analysis
52 include deep tissues within and behind the lamina cribrosa and feeder vessels in the peripapillary

53 sclera. Based on the reconstructed vascular network, we measured for each vessel segment four
54 geometric parameters: length, tortuosity, inclination, and polar orientation. The workflow
55 demonstrated herein is a prerequisite to assess the hemodynamic environment within the ONH,
56 which will help clarify the underlying mechanisms of retinal ganglion cell axon damage in
57 ischemic-related ocular diseases such as glaucoma.

58 **2. Methods**

59 First, we reconstructed the 3D vascular network of the ONH following the general procedure
60 shown in **Figure 2A**. Then, we characterized four geometric parameters for each of the vessel
61 segments: length, tortuosity, inclination, and polar orientation. The steps are described in detail
62 below.

63 **2.1 Vessel labeling**

64 All procedures were approved by the University of Pittsburgh's Institutional Animal Care and Use
65 Committee (IACUC), and adhered to both the guidelines set forth in the National Institute of
66 Health's Guide for the Care and Use of Laboratory Animals and the Association of Research in
67 Vision and Ophthalmology Statement for the use of animals in ophthalmic and vision research
68 [30].

69 The head of a healthy 15-year-old female rhesus macaque monkey was received within
70 30 minutes of sacrifice. Two polyimide micro-catheters (Docol Inc., Sharon, MA) were inserted
71 into the carotid arteries on each side of the neck. The vascular bed was washed with warm
72 phosphate-buffered saline. To avoid vessel damage, the phosphate-buffered saline perfusion
73 pressure was first minimal, and then progressively increased over several minutes as the output
74 solution cleared. Phosphate-buffered saline was washed for at least 10 minutes after the output
75 was clear. The anterior chamber of each eye was cannulated to control intraocular pressure using
76 an isotonic saline fluid column. The intraocular pressure was set to 5 mmHg throughout the
77 experiment. The level was selected as a compromise to be as low as possible to minimize
78 intraocular pressure-induced vessel closure, without being so low as to causing buckling or
79 hypotony that could distort the tissues. Dil, a lipophilic carbocyanine dye, was used to label
80 vessels in the eye [31]. We perfused 100 mL of aqueous Dil solution into each carotid artery at a
81 rate of 5-10 mL/min until the whole solution had been used (about 12 min), followed by another
82 phosphate-buffered saline wash to remove residual Dil.

83 We then perfused 50 mL of 10% formalin into each carotid artery twice, with an interval of
84 15 minutes, while maintaining intraocular pressure at 5 mmHg. After an additional 15 minutes,
85 both eyes were enucleated, making sure to preserve optic nerves at least 5 mm in length from
86 the globe. The intraocular pressure control lines were switched from saline to 10% formalin
87 columns. To complete the fixation, both eyes were immersion fixed overnight in 10% formalin
88 while the intraocular pressure was maintained at 5 mmHg.

89 The right eye was hemisected, and the retina was examined under a dissecting fluorescence
90 microscope (Olympus MVX10, Olympus, Tokyo, Japan) to evaluate vessel labeling. Although a
91 perfectly labeled retina is not equivalent to a perfectly labeled ONH, perfusion problems often
92 show up in both regions and they are easier to spot in the retina. The image shows continuous
93 staining of the retinal vasculature without any discernible dark patches or leaks (**Figure 2B**),
94 indicating the eye had satisfactory perfusions.

95 **2.2 Histology and imaging**

96 The ONH and surrounding sclera were isolated using a 14-mm-diameter circular trephine. The
97 tissues were placed in 30% sucrose overnight for cryoprotection, flash-frozen in optimum cutting
98 temperature compound (Tissue Plus, Fisher Healthcare, Houston, TX), and sectioned coronally
99 at 16 μm thickness with a cryostat (Leica CM3050S) [32, 33]. Both fluorescence microscopy (FM)
100 and instant polarized light microscopy (IPOL) images were then acquired of each section using a
101 commercial inverted microscope (IX83, Olympus, Tokyo, Japan) to visualize the vessels and
102 collagen, respectively. Note that each FM/IPOL image pair was co-localized to each other as they
103 were acquired right after the other separated only by the motorized filter switch. A 4x strain-free
104 objective (UPLFLN 4XP, Olympus, Tokyo, Japan) was used for both FM and IPOL. A Cy3/TRITC
105 filter set (545/605 nm, Olympus U-3N49004) was used for FM to match the excitation/emission
106 profiles of Dil. IPOL was implemented as described recently [34].

107 **2.3 3D vascular network reconstruction**

108 The stack of IPOL images was registered as described elsewhere [35, 36]. Briefly, this was done
109 manually using Avizo (version 9.1, FEI; Thermo Fisher Scientific) based on tissue edges and
110 fiducial marks made on the sclera and dura prior to embedding. The set of transformations
111 (translations and rotation) from the IPOL stack registration were then applied to the FM image
112 stack. Thus, an FM/IPOL image pair remained co-localized. A 3D rendered volume of the ONH
113 vasculature is shown in **Figure 3**. In addition, we identified the location of the lamina cribrosa
114 based on the registered IPOL images [33, 37]. Since the FM/IPOL image stacks were co-localized,
115 the location of the lamina cribrosa identified from IPOL images can be applied to the FM images
116 to identify the vessels in the lamina cribrosa [38].

117 The registered set of FM images was segmented (**Figure 4**) using a semi-automated
118 algorithm based on the Hessian-based Frangi vesselness filter and hysteresis thresholding [39-
119 41]. The binarized images were carefully checked and small corrections applied if necessary.
120 These were, for example, at some vessel bifurcations because the Frangi filter parameters were
121 selected to optimize accuracy in the main vessel segments and therefore sometimes led to minor

122 over or under-segmentations in bifurcations. Also, because the fluorescent label marked the
123 tissues of the wall, not the lumen, sometimes we had to “fill-in” the vessel. After reconstruction we
124 did a second evaluation of the vessels, checking for continuity and especially for any indication
125 that there may have been clots, poor labeling or leaks that could have affected the visualization
126 and reconstruction. We observed that sometimes vessel segments exhibited uneven brightness,
127 individually, or as a small region, but these were not difficult to identify and mark reliably once the
128 stack had been assembled. Again, for us to consider the perfusion satisfactory, as was the case
129 for the eye presented in this manuscript, there had to be no evidence of mislabeled vessels (dark
130 patches) or dye leaks in the vasculature. We recognize that there will always be some degree of
131 uncertainty about the methods and whether these guarantee that every blood vessel is captured.
132 We address this in the discussion.

133 The vessel network was then skeletonized using the built-in “Auto Skeletonization” algorithm
134 in Avizo (version 9.1, FEI; ThermoScientific) and converted into a 3D graph, with all vessels
135 connected except at the boundaries of the vascular network (**Figure 5**). This was done in a semi-
136 automatic iterative process that included segmentation and skeletonization, followed by an
137 analysis and detailed inspection of the skeleton. The results from this analysis guided an improved
138 re-segmentation and re-skeletonization. This sometimes required multiple iterations until we were
139 satisfied that the reconstruction was free of potential artifacts while remaining true to the
140 fluorescence images indicating the vasculature. We identified the vessels in the lamina cribrosa
141 region based on the presence of collagen beams [33, 37]. The terminal points at the boundaries
142 of the vascular network were grouped based on the anatomic characteristics of the ONH. [10, 42]
143 The terminal points were labeled according to their location and likely role. For example, vessel
144 terminal points at the canal periphery are thought to correspond to blood flow inlets from the
145 feeder vessels in the peripapillary sclera [28, 43, 44]. Conversely, vessel terminal points at the
146 center are thought to correspond with outlets for blood drainage through the central retinal vein.
147 [43] Terminal points at the anterior and posterior boundaries of the reconstructed volume
148 correspond with anastomoses directly linking the region with the pre-laminar and retro-laminar
149 regions.

150 **2.4 Quantification of vascular geometry**

151 Each vessel segment was defined as an unbranched tract between two branch points or between
152 a branch point and a terminal point. We characterized four geometric parameters of the segments:
153 length, tortuosity, inclination, and polar orientation. The parameter definitions are illustrated in
154 **Figure 6**. The implications of these parameters are detailed in the Discussion.

155 **3. Results**

156 The 3D reconstructed vascular network of the ONH is shown in **Figure 7**, with the vessels in the
157 lamina cribrosa region highlighted. The entire vascular network consisted of 12,966 vessel
158 segments, 7,989 branching points, and 1,100 terminal points at the network boundaries.
159 Specifically, the numbers of terminal points at the periphery, center, pre-laminar, and retro-laminar
160 boundaries were 409, 53, 159, and 479, respectively.

161 The quantitative analysis of the four geometric parameters of the vessels of the entire ONH is
162 shown in **Figure 8**. No obvious spatial patterns emerged when we visualized the vessels colored
163 according to each of the parameters, although it was possible to fit well functional forms to the
164 frequency distribution of each of the parameters. The frequency histograms show that the majority
165 of vessels were short and fairly straight, and primarily oriented towards the coronal plane. The
166 difference in the frequency between the radially and circumferentially aligned vessels was minimal.
167 The quartiles and functional fits of each parameter are summarized in **Table 1**.

168

169 4. Discussion

170 Our goal was to introduce a workflow that allows reconstruction and morphological analysis of the
171 3D vascular network of the ONH, including deep tissues within and behind the lamina cribrosa,
172 and feeder vessels from the peripapillary sclera. We have described the workflow and
173 demonstrated that it could be used successfully by showing the 3D reconstruction of the vessels
174 of a monkey ONH. Analysis of the vessels reveals information on the vessel length, tortuosity,
175 inclination, and polar orientation that has not been available from previous techniques. This
176 information is essential to understand ONH hemodynamics and its potential role in physiology,
177 pathology, and vision loss. Before we go any further, we remind readers that the measurements
178 reported herein were obtained from a single eye, and thus that it is impossible to know how
179 general they are. More eyes must be studied before general conclusions can be drawn. Our intent
180 in this work was to illustrate the workflow and the value that it brings to the study of ONH
181 architecture and hemodynamics. We are not aware of publications providing the detailed
182 information on ONH vessels that we report. Below we discuss our findings concerning each
183 geometric parameter, why they are important and worthy of study, and suggest potential
184 implications if the findings indeed generalize.

185 *Tortuosity* followed an exponential distribution. A comparison of the vessel tortuosity in the
186 ONH with other vascular beds is shown in **Table 2**. We found that the vessel tortuosity in the
187 monkey ONH, as measured herein, was similar to that in the pig lamina cribrosa [2], the mouse
188 brain [45], and the human retina [46] and kidney [47], but smaller than that in the human spleen
189 [47]. Most vessels in the network were fairly straight, but tortuous vessels also existed. Blood flow
190 in tortuous vessels is often lower than that in straight ones, particularly for large vessels; however,
191 tortuous vessels may have some advantages. First, increased tortuosity may bring vessels into
192 closer proximity to the tissues that they nourish, improving overall nutrition and oxygen exchange
193 [48]. Second, vessel tortuosity may provide “slack” that mitigates against reduced blood flow and
194 structural damage caused by excessive distortion under elevated intraocular pressure or changes
195 in gaze position [2, 49]. Thus, it seems reasonable that the ONH will exhibit a mix of tortuous and
196 straight vessels, depending on the local needs and biomechanical environment.

197 Note that tortuosity is a relative concept. A vessel with tortuosity of 1.0 is straight. Otherwise,
198 it has some tortuosity. Values of tortuosity that determine if a vessel is considered tortuous or not
199 are thus potentially different between tissues or conditions. As shown in Table 2, vessel tortuosity
200 in this work is in line with vessel tortuosity in other tissues and species. Whether vessel tortuosity

201 contributes to make the ONH more susceptible to reduced perfusion or hypoxia is still unknown
202 as it will depend on a large number of factors.

203 *Vessel length* followed a lognormal distribution with skewness larger than 1. This means that
204 the majority of vascular lengths were shorter than the mean length. A network formed by short
205 vessels may be more interconnected and robust to vascular occlusion than one formed by long
206 vessels. A comparison of the vessel length in the ONH with other vascular beds is shown in
207 **Figure 9**.

208 *Inclination* followed a logistic curve. The curve increased rapidly from 0° to 45°, and smoothly
209 thereafter. There was a spike at 90°. The spike likely results from using a relatively thick section
210 (16 μm) to reconstruct the vascular network. This is discussed in more detail later. In terms of the
211 implications, it seems reasonable to expect that vessel sensitivity to mechanical insult depends
212 on the relative orientations of the insult and the vessel [50, 51]. For instance, a vessel
213 compression in the direction perpendicular to its axis might result in a larger flow reduction than
214 a compression longitudinally. Thus, if the ONH is subjected to intraocular pressure-related
215 compression along the anterior-posterior direction [52-55], vessels oriented in the coronal plane
216 (perpendicular to the compressive insult) may be affected more than vessels oriented in the
217 anterior-posterior direction.

218 The inclination of the ONH vessels may also influence their visibility in imaging. This is crucial
219 to consider because many of the techniques available for imaging the ONH vasculature in vivo
220 have biases in the vessel visibility and flow measurement sensitivity depending on the vessel
221 inclination. For instance, techniques based on doppler have maximum sensitivity when the vessel
222 (and flow) axis is aligned with the imaging axis. When imaged from the front, as is most common
223 in optical coherence tomography angiography and ultrasound, the techniques would preferentially
224 visualize anterior-posterior vessels and flow [56-58]. Conversely, techniques based on speckle
225 autocorrelation are thought to have higher resolving power in the plane perpendicular to the laser
226 beam, and thus may better visualize vessels and flow in the coronal plane [59-61]. Therefore, a
227 better understanding of the inclination of the ONH vessels is crucial for properly interpreting in
228 vivo data.

229 *Polar orientation* followed a nearly uniform distribution. The difference in the frequency
230 between the radially and circumferentially aligned vessels was minimal. Such a slight difference
231 is unlikely to be biomechanically meaningful and impactful. Our finding suggests that the
232 circumferential flow may be as substantial as the radial one. This may facilitate blood circulation

233 in the ONH region, and potentially make it more robust to compression-induced blockage. Our
234 statements about flow and robustness, however, are speculation and must be verified.

235 We believe that there are many potential applications of our work. We would like to highlight
236 four: First, the 3D reconstructed vascular network will allow modeling eye-specific ONH blood flow
237 and oxygen concentration. This would be more physiologically accurate than what can be
238 considered in 2D generic models [50, 51, 62, 63]. Our reconstructions and analysis will allow
239 evaluating the physiological accuracy of simplified/generic models, and development of improved
240 ones. Second, the models derived from our vascular network can be used to understand the
241 effects on ONH hemodynamics of tissue distortions, for instance, due to changes in intraocular
242 pressure or cerebrospinal fluid pressure, or due to changes in gaze position [49, 53, 64, 65].
243 Predictions made with detailed specimen-specific models can then be better compared with
244 experimental data than generic models. Third, our integrated imaging technique, *i.e.*, FM and
245 IPOL, allowed us to reconstruct both the vessels and collagen in the ONH. It is thus possible to
246 evaluate the spatial relationship between the vascular and collagenous networks. Other vessel
247 visualization techniques, such as plastic casts, have required “digestion” of the tissues for
248 visualization [28, 29]. This makes it impossible to determine accurately the inter-relationship
249 between vessels and non-vessels tissues. The combined vessels and collagen information from
250 our workflow allows precisely locating the vessels. This, in turn, allows distinguishing vessels
251 inside/outside the canal, and vessels within or outside lamina cribrosa collagen beams. These
252 will likely have important implications on the sensitivity of the vessels to distortion and their
253 proximity to the neural tissues [38]. Fourth, the techniques for visualizing and characterizing ONH
254 vasculature *in vivo* have major limitations. The reconstructions and morphologic parameters from
255 our workflow can provide the essential “ground truth” to assess and optimize other techniques.
256 All of these applications will benefit from the detailed reconstruction methods we present and are
257 evidence of the great potential that our technique has to help understand the interactions between
258 morphological, hemodynamic, and biomechanical factors influencing blood flow and oxygenation
259 in the ONH.

260 It is important to acknowledge the limitations to this work. A salient one, noted above, is that
261 we have presented measurements from a single eye. Our work therefore serves as a
262 demonstration of what can be done. Although our measures of the vessel tortuosity and length
263 were generally consistent with those of other vascular beds, our numbers were obtained from a
264 single ONH. Given the high inter-eye variability in other aspects of ONH morphology, readers
265 should be cautious and not assume that our findings are general. There are also limitations of the

266 3D vascular network reconstruction workflow. Dye perfusion post-mortem may not reach all
267 vessel segments. This could result from intravascular clotting or insufficient perfusate volume. To
268 prevent intravascular clotting, efforts were made to minimize the time interval between animal
269 death and perfusion. In addition, the vessels were flushed with extensive PBS over a long time to
270 remove the residual blood clots. To ensure sufficient labeling, we used a large volume of dye to
271 perfuse. The examination using a dissecting fluorescence microscope showed strong
272 fluorescence signals in retinal and choroidal vessels, suggesting sufficient vessel perfusion. We
273 did not observe gaps or recognize regions blocked by clots, which does not mean that they did
274 not exist, but does strongly suggest that they would be small and not abundant. It is worth noting
275 that other ex vivo perfusion techniques have equivalent or worse risks. For example, vascular
276 casting is well-known to be affected by the solution viscosity that may prevent full perfusion into
277 smaller vessels [28, 29].

278 Artifacts may result from fixation or sectioning, including tissue distortion or shrinkage.
279 However, we have shown previously that our method of formalin fixation has minimal effects on
280 the gross size or shape of ocular tissues [32, 33]. It is unclear how it may affect the vasculature
281 within. Artifacts may also result from registering histological section images. We could have used
282 the central retinal vessels in the FM as continuous vascular features for registration. However, we
283 were worried that this could lead to artefactually aligning other vessels in these images. To avoid
284 this problem, we registered the stacks using the IPOL images of collagen. Specifically, we used
285 the tissue edges and other recognizable structures to align them, and then applied the set of
286 transformations from the IPOL stack registration to the FM image stack. This process is time-
287 consuming and may introduce misalignment due to subjective evaluation of the registration. We
288 could use fiducial markers to help register images and account for warping [66]. Note that these
289 artifacts are not necessarily worse and are potentially smaller than with other imaging techniques.
290 For example, in vivo optical coherence tomography suffers substantial artifacts caused by motion,
291 projections of superficial blood flow or shadows from opaque objects anterior to the retina (e.g.,
292 vitreous floaters, pupil boundary) [67].

293 Artifacts may also result from the skeletonization step. **Unevenly or sometimes slightly**
294 **discontinuous labeling increased the difficulty in segmentation. Hessian filter and hysteresis**
295 **thresholding provided excellent starting points for vessel contour enhancement but with limited**
296 **success on uneven labels and at anastomoses. Therefore, it was still necessary to manually**
297 **“clean” and “bridge” segments. Particularly, time consuming was identifying and cleaning out-of-**
298 **plane vessel discontinuities. It was also crucial to ensure the smoothness of the segmentations**

299 because these impact the skeletonization. Intervening on this could potentially affect the vessel
300 widths or diameters, and therefore we decided to not report vessel diameters. Problems with the
301 skeletonization often lead to many artefactual short segments forming small loops or fanning out.
302 These were not observed in the skeletonization reported herein, in large part because of our use
303 of an iterative algorithm that ensured they were eliminated. However, the general problem of
304 skeletonization in 3D remains a challenge and the same algorithm can perform differently in other
305 images and networks. Future studies should be careful and not assume that the skeletonization
306 is accurate.

307 As noted above, the section thickness may affect the reconstructions, and it is thus an
308 important consideration. When choosing thickness, there are tradeoffs between the advantages
309 of thick and thin sections. Thicker sections suffer less from distortion and reduce the workload.
310 Thinner sections allow more detailed reconstruction, allowing distinguishing better the vessel
311 plane and especially the inclination of short vessels. In this study, the section thickness was
312 chosen as 16 μm , resulting in 58 sections through the monkey ONH. Of these, 29 sections were
313 selected for reconstruction. With this depth resolution, any two vessels with a gap distance of less
314 than 16 μm in depth were connected, and vessels shorter than 45 μm and an inclination of more
315 than 80° were regarded as in the coronal plane. This explains the sharp increase in vessel
316 frequency at 90° inclination (in the section plane). Reducing the section thickness would improve
317 the fidelity of the 3D reconstructed vascular network. For example, techniques like a tape transfer
318 system can be used to reduce the minimal section thickness to single digit μm [68]. Alternatively,
319 future work could use techniques that can provide depth information, such confocal microscopy,
320 or structured light illumination [2, 53]. There are also block face imaging and serial electron
321 microscopy tools that can provide exquisite resolution in the order of nm [69, 70]. Those
322 techniques, however, tend to be substantially slower and expensive and thus are rarely used for
323 analyzing a large set of sections as we have done here.

324 Our analysis did not provide information on the vessel diameters. Post-mortem vessel
325 diameter may differ from that in vivo due to the absence of blood pressure and/or tissue swelling
326 post-mortem. An additional challenge is that many vessels are inside the connective tissue beams
327 [2], which may further complicate the diameter changes post mortem. Inside the micromechanical
328 environment of collagenous beams, the diameter of vasculature may be related to the sensitivity
329 of perfusion when intraocular pressure changes. Future work could examine this issue using other
330 methods to label vessels of the ONH, which may potentially require more complex and specific
331 labeling techniques, and likely slower imaging.

332 Overall, we demonstrated a histological imaging workflow allowing reconstruction and
333 morphological analysis of the 3D vascular network of the ONH. A similar approach can be used
334 to reconstruct vascular networks in eyes of different ages and diseased eyes to further understand
335 age- and disease-related morphological changes in the ONH vasculature.

336 **Acknowledgements**

337 Supported by National Institutes of Health R01-EY023966, R01-EY028662, R01-EY031708, R01-
338 HD045590, R01-HD083383, P30-EY008098, and T32-EY017271; Eye and Ear Foundation
339 (Pittsburgh, Pennsylvania), Research to Prevent Blindness.

340 **References**

- 341 [1] Stein, J.D., Khawaja, A.P., and Weizer, J.S., 2021, "Glaucoma in Adults—Screening,
342 Diagnosis, and Management: A Review," *JAMA*, 325(2), pp. 164-174.
343 <https://doi.org/10.1001/jama.2020.21899>.
- 344 [2] Brazile, B.L., Yang, B., Waxman, S., Lam, P., Voorhees, A.P., Hua, Y., Loewen, R.T.,
345 Loewen, N.A., Rizzo III, J.F., Jakobs, T.C., and Sigal, I.A., 2020, "Lamina cribrosa
346 capillaries straighten as intraocular pressure increases," *Investigative Ophthalmology &
347 Visual Science*, 61(12), pp. 2-2. <https://doi.org/10.1167/iovs.61.12.2>.
- 348 [3] Lieberman, M.F., Maumenee, A.E., and Green, W.R., 1976, "Histologic studies of the
349 vasculature of the anterior optic nerve," *American journal of ophthalmology*, 82(3), pp.
350 405-423. [https://doi.org/10.1016/0002-9394\(76\)90489-x](https://doi.org/10.1016/0002-9394(76)90489-x).
- 351 [4] Zhang, L., Albon, J., Jones, H., Gouget, C.L., Ethier, C.R., Goh, J.C., and Girard, M.J.,
352 2015, "Collagen microstructural factors influencing optic nerve head biomechanics,"
353 *Investigative ophthalmology & visual science*, 56(3), pp. 2031-2042.
354 <https://doi.org/10.1167/iovs.14-15734>.
- 355 [5] Midgett, D.E., Jefferys, J.L., Quigley, H.A., and Nguyen, T.D., 2020, "The inflation
356 response of the human lamina cribrosa and sclera: Analysis of deformation and
357 interaction," *Acta Biomaterialia*, 106(1), pp. 225-241.
358 <https://doi.org/10.1016/j.actbio.2020.01.049>.
- 359 [6] Pavlatos, E., Ma, Y., Clayson, K., Pan, X., and Liu, J., 2018, "Regional deformation of the
360 optic nerve head and peripapillary sclera during IOP elevation," *Investigative
361 ophthalmology & visual science*, 59(8), pp. 3779-3788. [https://doi.org/10.1167/iovs.18-
362 24462](https://doi.org/10.1167/iovs.18-24462).
- 363 [7] Voorhees, A.P., Jan, N.-J., Austin, M.E., Flanagan, J.G., Sivak, J.M., Bilonick, R.A., and
364 Sigal, I.A., 2017, "Lamina cribrosa pore shape and size as predictors of neural tissue
365 mechanical insult," *Investigative ophthalmology & visual science*, 58(12), pp. 5336-5346.
366 <https://doi.org/10.1167/iovs.17-22015>.
- 367 [8] Voorhees, A.P., Jan, N.-J., and Sigal, I.A., 2017, "Effects of collagen microstructure and
368 material properties on the deformation of the neural tissues of the lamina cribrosa," *Acta
369 biomaterialia*, 58, pp. 278-290. <https://doi.org/10.1016/j.actbio.2017.05.042>.
- 370 [9] Quigley, H.A., 2005, "Glaucoma: macrocosm to microcosm the Friedenwald lecture,"
371 *Investigative ophthalmology & visual science*, 46(8), pp. 2663-2670.
372 <https://doi.org/10.1167/iovs.04-1070>.
- 373 [10] Sigal, I.A., and Ethier, C.R., 2009, "Biomechanics of the optic nerve head," *Experimental
374 eye research*, 88(4), pp. 799-807. <https://doi.org/10.1016/j.exer.2009.02.003>.
- 375 [11] Harris, A., Kagemann, L., Ehrlich, R., Rospigliosi, C., Moore, D., and Siesky, B., 2008,
376 "Measuring and interpreting ocular blood flow and metabolism in glaucoma," *Canadian
377 Journal of Ophthalmology*, 43(3), pp. 328-336. <https://doi.org/10.3129/i08-051>.
- 378 [12] Moore, D., Harris, A., Wudunn, D., Kheradiya, N., and Siesky, B., 2008, "Dysfunctional
379 regulation of ocular blood flow: A risk factor for glaucoma?," *Clinical ophthalmology
380 (Auckland, N.Z.)*, 2(4), pp. 849-861. <https://doi.org/10.2147/opth.s2774>.
- 381 [13] Galassi, F., Giambene, B., and Varriale, R., 2011, "Systemic vascular dysregulation and
382 retrobulbar hemodynamics in normal-tension glaucoma," *Investigative Ophthalmology &
383 Visual Science*, 52(7), pp. 4467-4471. <https://doi.org/10.1167/iovs.10-6710>.
- 384 [14] Kanakamedala, P., Harris, A., Siesky, B., Tying, A., Muchnik, M., Eckert, G., and Tobe,
385 L.A., 2014, "Optic nerve head morphology in glaucoma patients of African descent is
386 strongly correlated to retinal blood flow," *British Journal of Ophthalmology*, 98(11), pp.
387 1551-1554. <https://doi.org/10.1136/bjophthalmol-2013-304393>.
- 388 [15] Hayreh, S.S., 1997, "Factors influencing blood flow in the optic nerve head," *Journal of
389 glaucoma*, 6(6), pp. 412-425.

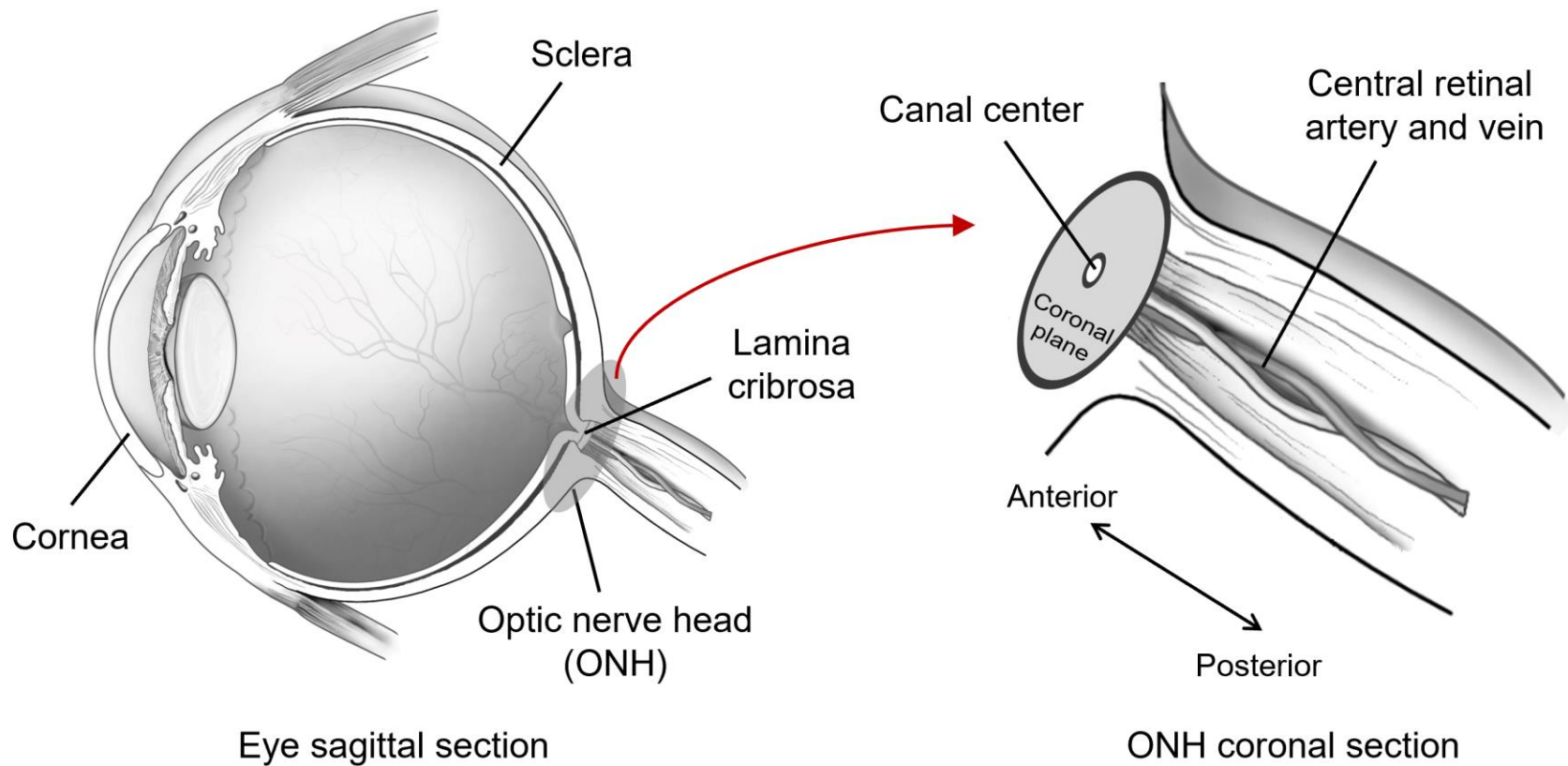
- 390 [16] Sigal, I.A., Wang, B., Strouthidis, N.G., Akagi, T., and Girard, M.J., 2014, "Recent
391 advances in OCT imaging of the lamina cribrosa," *British Journal of Ophthalmology*,
392 98(Suppl 2), pp. ii34-ii39. <https://doi.org/10.1136/bjophthalmol-2013-304751>.
- 393 [17] Numa, S., Akagi, T., Uji, A., Suda, K., Nakanishi, H., Kameda, T., Ikeda, H.O., and
394 Tsujikawa, A., 2018, "Visualization of the lamina Cribrosa microvasculature in normal and
395 glaucomatous eyes: a Swept-source optical coherence tomography angiography study,"
396 *Journal of Glaucoma*, 27(11), pp. 1032-1035.
397 <https://doi.org/10.1097/IJG.0000000000001069>.
- 398 [18] Zhu, J., Bernucci, M.T., Merkle, C.W., and Srinivasan, V.J., 2020, "Visibility of
399 microvessels in Optical Coherence Tomography Angiography depends on angular
400 orientation," *Journal of Biophotonics*, 13(10), p. e202000090.
401 <https://doi.org/10.1002/jbio.202000090>.
- 402 [19] Kim, J.-A., Lee, E.J., Kim, T.-W., Yang, H.K., and Hwang, J.-M., 2021, "Comparison of
403 Optic Nerve Head Microvasculature Between Normal-Tension Glaucoma and Nonarteritic
404 Anterior Ischemic Optic Neuropathy," *Investigative Ophthalmology & Visual Science*,
405 62(10), pp. 15-15. <https://doi.org/10.1167/iovs.62.10.15>.
- 406 [20] Yu, J., Lavery, L., and Kim, K., 2018, "Super-resolution ultrasound imaging method for
407 microvasculature in vivo with a high temporal accuracy," *Scientific reports*, 8(1), pp. 1-11.
408 <https://doi.org/10.1038/s41598-018-32235-2>.
- 409 [21] Christensen-Jeffries, K., Couture, O., Dayton, P.A., Eldar, Y.C., Hynynen, K., Kiessling,
410 F., O'Reilly, M., Pinton, G.F., Schmitz, G., and Tang, M.-X., 2020, "Super-resolution
411 ultrasound imaging," *Ultrasound in Medicine & Biology*, 46(4), pp. 865-891.
412 <https://doi.org/10.1016/j.ultrasmedbio.2019.11.013>.
- 413 [22] Chen, Q., Yu, J., Lukashova, L., Latoche, J.D., Zhu, J., Lavery, L., Verdelis, K., Anderson,
414 C.J., and Kim, K., 2020, "Validation of ultrasound super-resolution imaging of vasa
415 vasorum in rabbit atherosclerotic plaques," *IEEE Transactions on Ultrasonics,*
416 *Ferroelectrics, and Frequency Control*, 67(8), pp. 1725-1729.
417 <https://doi.org/10.1109/TUFFC.2020.2974747>.
- 418 [23] Qian, X., Kang, H., Li, R., Lu, G., Du, Z., Shung, K.K., Humayun, M.S., and Zhou, Q., 2020,
419 "In vivo visualization of eye vasculature using super-resolution ultrasound microvessel
420 imaging," *IEEE Transactions on Biomedical Engineering*.
421 <https://doi.org/10.1109/TBME.2020.2972514>.
- 422 [24] Duong, T.Q., Pardue, M.T., Thulé, P.M., Olson, D.E., Cheng, H., Nair, G., Li, Y., Kim, M.,
423 Zhang, X., and Shen, Q., 2008, "Layer-specific anatomical, physiological and functional
424 MRI of the retina," *NMR in Biomedicine: An International Journal Devoted to the*
425 *Development and Application of Magnetic Resonance In vivo*, 21(9), pp. 978-996.
426 <https://doi.org/10.1002/nbm.1311>.
- 427 [25] Voorhees, A.P., Ho, L.C., Jan, N.-J., Tran, H., van der Merwe, Y., Chan, K., and Sigal,
428 I.A., 2017, "Whole-globe biomechanics using high-field MRI," *Experimental eye research*,
429 160, pp. 85-95. <https://doi.org/10.1016/j.exer.2017.05.004>.
- 430 [26] Ho, L.C., Sigal, I.A., Jan, N.-J., Squires, A., Tse, Z., Wu, E.X., Kim, S.-G., Schuman, J.S.,
431 and Chan, K.C., 2014, "Magic angle-enhanced MRI of fibrous microstructures in sclera
432 and cornea with and without intraocular pressure loading," *Investigative Ophthalmology &*
433 *Visual Science*, 55(9), pp. 5662-5672. <https://doi.org/10.1167/iovs.14-14561>.
- 434 [27] Ho, L.C., Sigal, I.A., Jan, N.-J., Yang, X., Van Der Merwe, Y., Yu, Y., Chau, Y., Leung,
435 C.K., Conner, I.P., and Jin, T., 2016, "Non-invasive MRI assessments of tissue
436 microstructures and macromolecules in the eye upon biomechanical or biochemical
437 modulation," *Scientific reports*, 6, p. 32080. <https://doi.org/10.1038/srep32080>.
- 438 [28] Mackenzie, P.J., and Cioffi, G.A., 2008, "Vascular anatomy of the optic nerve head,"
439 *Canadian Journal of Ophthalmology*, 43(3), pp. 308-312. <https://doi.org/10.3129/i08-042>.

- 440 [29] Zhao, D.-Y., and Cioffi, G.A., 2000, "Anterior optic nerve microvascular changes in human
441 glaucomatous optic neuropathy," *Eye*, 14(3), pp. 445-449.
442 <https://doi.org/10.1038/eye.2000.129>.
- 443 [30] "Statement for the Use of Animals in Ophthalmic and Vision Research," The Association
444 for Research in Vision and Ophthalmology, last modified Fall 2016,
445 [https://www.arvo.org/About/policies/statement-for-the-use-of-animals-in-ophthalmic-and-](https://www.arvo.org/About/policies/statement-for-the-use-of-animals-in-ophthalmic-and-vision-research/)
446 [vision-research/](https://www.arvo.org/About/policies/statement-for-the-use-of-animals-in-ophthalmic-and-vision-research/).
- 447 [31] Li, Y., Song, Y., Zhao, L., Gaidosh, G., Laties, A.M., and Wen, R., 2008, "Direct labeling
448 and visualization of blood vessels with lipophilic carbocyanine dye Dil," *Nature protocols*,
449 3(11), pp. 1703-1708. <https://doi.org/10.1038/nprot.2008.172>.
- 450 [32] Tran, H., Jan, N.-J., Hu, D., Voorhees, A., Schuman, J.S., Smith, M.A., Wollstein, G., and
451 Sigal, I.A., 2017, "Formalin fixation and cryosectioning cause only minimal changes in
452 shape or size of ocular tissues," *Scientific Reports*, 7(1), pp. 1-11.
453 <https://doi.org/10.1038/s41598-017-12006-1>.
- 454 [33] Jan, N.-J., Grimm, J.L., Tran, H., Lathrop, K.L., Wollstein, G., Bilonick, R.A., Ishikawa, H.,
455 Kagemann, L., Schuman, J.S., and Sigal, I.A., 2015, "Polarization microscopy for
456 characterizing fiber orientation of ocular tissues," *Biomedical optics express*, 6(12), pp.
457 4705-4718. <https://doi.org/10.1364/BOE.6.004705>.
- 458 [34] Yang, B., Lee, P.-Y., Hua, Y., Brazile, B., Waxman, S., Ji, F., Zhu, Z., and Sigal, I.A., 2021,
459 "Instant polarized light microscopy for imaging collagen microarchitecture and dynamics,"
460 *Journal of Biophotonics*, 14(2), p. e202000326. <https://doi.org/10.1002/jbio.202000326>.
- 461 [35] Gogola, A., Jan, N.-J., Lathrop, K.L., and Sigal, I.A., 2018, "Radial and circumferential
462 collagen fibers are a feature of the peripapillary sclera of human, monkey, pig, cow, goat,
463 and sheep," *Investigative ophthalmology & visual science*, 59(12), pp. 4763-4774.
464 <https://doi.org/10.1167/iovs.18-25025>.
- 465 [36] Jan, N.-J., Brazile, B.L., Hu, D., Grube, G., Wallace, J., Gogola, A., and Sigal, I.A., 2018,
466 "Crimp around the globe; patterns of collagen crimp across the corneoscleral shell,"
467 *Experimental eye research*, 172, pp. 159-170. <https://doi.org/10.1016/j.exer.2018.04.003>.
- 468 [37] Jan, N.-J., Lathrop, K., and Sigal, I.A., 2017, "Collagen architecture of the posterior pole:
469 high-resolution wide field of view visualization and analysis using polarized light
470 microscopy," *Investigative ophthalmology & visual science*, 58(2), pp. 735-744.
471 <https://doi.org/10.1167/iovs.16-20772>.
- 472 [38] Waxman, S., Brazile, B.L., Yang, B., Lee, P.-Y., Hua, Y., Gogola, A.L., Lam, P., Voorhees,
473 A.P., Rizzo III, J.F., and Jakobs, T.C., 2021, "Lamina cribrosa vessel and collagen beam
474 networks are distinct," *Experimental Eye Research*, p. 108916.
475 <https://doi.org/10.1016/j.exer.2021.108916>.
- 476 [39] Kroon, D.-J., 2009, "Hessian based Frangi Vesselness filter. MATLAB Central File
477 Exchange."
- 478 [40] Campbell, I.C., Coudrillier, B., Mensah, J., Abel, R.L., and Ethier, C.R., 2015, "Automated
479 segmentation of the lamina cribrosa using Frangi's filter: a novel approach for rapid
480 identification of tissue volume fraction and beam orientation in a trabeculated structure in
481 the eye," *Journal of The Royal Society Interface*, 12(104), p. 20141009.
482 <https://doi.org/10.1098/rsif.2014.1009>.
- 483 [41] Jerman, T., Pernuš, F., Likar, B., and Špiclin, Ž., 2016, "Enhancement of vascular
484 structures in 3D and 2D angiographic images," *IEEE transactions on medical imaging*,
485 35(9), pp. 2107-2118. <https://doi.org/10.1109/TMI.2016.2550102>.
- 486 [42] Sigal, I.A., Flanagan, J.G., Tertinegg, I., and Ethier, C.R., 2010, "3D morphometry of the
487 human optic nerve head," *Experimental eye research*, 90(1), pp. 70-80.
488 <https://doi.org/10.1016/j.exer.2009.09.013>.

- 489 [43] Hayreh, S.S., 2001, "Blood flow in the optic nerve head and factors that may influence it,"
490 Progress in retinal and eye research, 20(5), pp. 595-624. [https://doi.org/10.1016/s1350-](https://doi.org/10.1016/s1350-9462(01)00005-2)
491 [9462\(01\)00005-2](https://doi.org/10.1016/s1350-9462(01)00005-2).
- 492 [44] Hayreh, S.S., 1996, "Blood supply of the optic nerve head," *Ophthalmologica*, 210(5), pp.
493 285-295. <https://doi.org/10.1159/000310727>.
- 494 [45] Hahn, A., Bode, J., Krüwel, T., Solecki, G., Heiland, S., Bendszus, M., Tews, B., Winkler,
495 F., Breckwoldt, M.O., and Kurz, F.T., 2019, "Glioblastoma multiforme restructures the
496 topological connectivity of cerebrovascular networks," *Scientific reports*, 9(1), pp. 1-17.
497 <https://doi.org/10.1038/s41598-019-47567-w>.
- 498 [46] Saraf, S.S., Tying, A.J., Chen, C.-L., Le, T.P., Kalina, R.E., Wang, R.K., and Chao, J.R.,
499 2019, "Familial retinal arteriolar tortuosity and quantification of vascular tortuosity using
500 swept-source optical coherence tomography angiography," *American journal of*
501 *ophthalmology case reports*, 14, pp. 74-78. <https://doi.org/10.1016/j.ajoc.2019.03.001>.
- 502 [47] Ágg, B., Szilveszter, B., Daradics, N., Benke, K., Stengl, R., Kolossváry, M., Pólos, M.,
503 Radovits, T., Ferdinandy, P., and Merkely, B., 2020, "Increased visceral arterial tortuosity
504 in Marfan syndrome," *Orphanet journal of rare diseases*, 15(1), pp. 1-10.
505 <https://doi.org/10.1186/s13023-020-01369-w>.
- 506 [48] Goldman, D., and Popel, A.S., 2000, "A computational study of the effect of capillary
507 network anastomoses and tortuosity on oxygen transport," *Journal of Theoretical Biology*,
508 206(2), pp. 181-194. <https://doi.org/10.1006/jtbi.2000.2113>.
- 509 [49] Sibony, P.A., Wei, J., and Sigal, I.A., 2018, "Gaze-evoked deformations in optic nerve
510 head drusen: repetitive shearing as a potential factor in the visual and vascular
511 complications," *Ophthalmology*, 125(6), pp. 929-937.
512 <https://doi.org/10.1016/j.ophtha.2017.12.006>.
- 513 [50] Chuangsuwanich, T., Hung, P.T., Wang, X., Liang, L.H., Schmetterer, L., Boote, C., and
514 Girard, M.J.A., 2020, "Morphometric, hemodynamic, and biomechanical factors
515 influencing blood flow and oxygen concentration in the human lamina cribrosa,"
516 *Investigative Ophthalmology & Visual Science*, 61(4), pp. 3-3.
517 <https://doi.org/10.1167/iovs.61.4.3>.
- 518 [51] Chuangsuwanich, T., Birgersson, K.E., Thiery, A., Thakku, S.G., Leo, H.L., and Girard,
519 M.J., 2016, "Factors influencing lamina cribrosa microcapillary hemodynamics and oxygen
520 concentrations," *Investigative Ophthalmology & Visual Science*, 57(14), pp. 6167-6179.
521 <https://doi.org/10.1167/iovs.16-20167>.
- 522 [52] Sigal, I.A., Flanagan, J.G., Tertinegg, I., and Ethier, C.R., 2007, "Predicted extension,
523 compression and shearing of optic nerve head tissues," *Experimental eye research*, 85(3),
524 pp. 312-322. <https://doi.org/10.1016/j.exer.2007.05.005>.
- 525 [53] Sigal, I.A., Grimm, J.L., Jan, N.J., Reid, K., Minckler, D.S., and Brown, D.J., 2014, "Eye-
526 specific IOP-induced displacements and deformations of human lamina cribrosa,"
527 *Investigative Ophthalmology & Visual Science*, 55(1), pp. 1-15.
528 <https://doi.org/10.1167/iovs.13-12724>.
- 529 [54] Ma, Y., Kwok, S., Sun, J., Pan, X., Pavlatos, E., Clayson, K., Hazen, N., and Liu, J., 2020,
530 "IOP-induced regional displacements in the optic nerve head and correlation with
531 peripapillary sclera thickness," *Experimental Eye Research*, 200, p. 108202.
532 <https://doi.org/10.1016/j.exer.2020.108202>.
- 533 [55] Ma, Y., Pavlatos, E., Clayson, K., Pan, X., Kwok, S., Sandwisch, T., and Liu, J., 2019,
534 "Mechanical deformation of human optic nerve head and peripapillary tissue in response
535 to acute IOP elevation," *Investigative ophthalmology & visual science*, 60(4), pp. 913-920.
536 <https://doi.org/10.1167/iovs.18-26071>.
- 537 [56] Yazdanfar, S., Rollins, A.M., and Izatt, J.A., 2000, "Imaging and velocimetry of the human
538 retinal circulation with color Doppler optical coherence tomography," *Optics Letters*,
539 25(19), pp. 1448-1450. <https://doi.org/10.1364/ol.25.001448>.

- 540 [57] Tranquart, F., Bergès, O., Koskas, P., Arsene, S., Rossazza, C., Pisella, P.J., and
541 Pourcelot, L., 2003, "Color Doppler imaging of orbital vessels: personal experience and
542 literature review," *Journal of Clinical Ultrasound*, 31(5), pp. 258-273.
543 <https://doi.org/10.1002/jcu.10169>.
- 544 [58] Harris, A., Kagemann, L., and Cioffi, G.A., 1998, "Assessment of human ocular
545 hemodynamics," *Survey of ophthalmology*, 42(6), pp. 509-533.
546 [https://doi.org/10.1016/s0039-6257\(98\)00011-3](https://doi.org/10.1016/s0039-6257(98)00011-3).
- 547 [59] Hormel, T.T., Huang, D., and Jia, Y., 2021, "Artifacts and artifact removal in optical
548 coherence tomographic angiography," *Quantitative Imaging in Medicine and Surgery*,
549 11(3), p. 1120. <https://doi.org/10.21037/qims-20-730>.
- 550 [60] Wang, L., Cull, G.A., Piper, C., Burgoyne, C.F., and Fortune, B., 2012, "Anterior and
551 posterior optic nerve head blood flow in nonhuman primate experimental glaucoma model
552 measured by laser speckle imaging technique and microsphere method," *Investigative
553 ophthalmology & visual science*, 53(13), pp. 8303-8309. <https://doi.org/10.1167/iovs.12-10911>.
- 554 [61] Liang, Y., Fortune, B., Cull, G., Cioffi, G.A., and Wang, L., 2010, "Quantification of dynamic
555 blood flow autoregulation in optic nerve head of rhesus monkeys," *Experimental eye
556 research*, 90(2), pp. 203-209. <https://doi.org/10.1016/j.exer.2009.10.009>.
- 557 [62] Causin, P., Guidoboni, G., Malgaroli, F., Sacco, R., and Harris, A., 2016, "Blood flow
558 mechanics and oxygen transport and delivery in the retinal microcirculation: multiscale
559 mathematical modeling and numerical simulation," *Biomechanics Modeling in
560 Mechanobiology*, 15(3), pp. 525-542. <https://doi.org/10.1007/s10237-015-0708-7>.
- 561 [63] Causin, P., Guidoboni, G., Harris, A., Prada, D., Sacco, R., and Terragni, S., 2014, "A
562 poroelastic model for the perfusion of the lamina cribrosa in the optic nerve head,"
563 *Mathematical biosciences*, 257, pp. 33-41. <https://doi.org/10.1016/j.mbs.2014.08.002>.
- 564 [64] Hua, Y., Voorhees, A.P., and Sigal, I.A., 2018, "Cerebrospinal fluid pressure: revisiting
565 factors influencing optic nerve head biomechanics," *Investigative ophthalmology & visual
566 science*, 59(1), pp. 154-165. <https://doi.org/10.1167/iovs.17-22488>.
- 567 [65] Zhu, Z., Waxman, S., Wang, B., Wallace, J., Schmitt, S.E., Tyler-Kabara, E., Ishikawa, H.,
568 Schuman, J.S., Smith, M.A., and Wollstein, G., 2021, "Interplay between intraocular and
569 intracranial pressure effects on the optic nerve head in vivo," *Experimental Eye Research*,
570 p. 108809. <https://doi.org/10.1016/j.exer.2021.108809>.
- 571 [66] Sigal, I.A., Flanagan, J.G., Tertinegg, I., and Ethier, C.R., 2005, "Reconstruction of human
572 optic nerve heads for finite element modeling," *Technology and Health Care*, 13(4), pp.
573 313-329. <https://doi.org/10.3233/THC-2005-13410>.
- 574 [67] Spaide, R.F., Fujimoto, J.G., and Waheed, N.K., 2015, "Image artifacts in optical
575 coherence angiography," *Retina (Philadelphia, Pa.)*, 35(11), p. 2163.
576 <https://doi.org/10.1097/IAE.0000000000000765>.
- 577 [68] Golubeva, Y.G., Smith, R.M., and Sternberg, L.R., 2013, "Optimizing frozen sample
578 preparation for laser microdissection: assessment of CryoJane tape-transfer system@,"
579 *PIOS ONE*, 8(6), p. e66854. <https://doi.org/10.1371/journal.pone.0066854>.
- 580 [69] Quantock, A.J., Winkler, M., Parfitt, G.J., Young, R.D., Brown, D.J., Boote, C., and Jester,
581 J.V., 2015, "From nano to macro: studying the hierarchical structure of the corneal
582 extracellular matrix," *Experimental eye research*, 133, pp. 81-99.
583 <https://doi.org/10.1016/j.exer.2014.07.018>.
- 584 [70] Boote, C., Sigal, I.A., Grytz, R., Hua, Y., Nguyen, T.D., and Girard, M.J., 2020, "Scleral
585 structure and biomechanics," *Progress in retinal and eye research*, 74, p. 100773.
586 <https://doi.org/10.1016/j.preteyeres.2019.100773>.
- 587 [71] Jafarnejad, M., Ismail, A., Duarte, D., Vyas, C., Ghahramani, A., Zawieja, D., Celso, C.L.,
588 Poologasundarampillai, G., and Moore, J., 2019, "Quantification of the whole lymph node
589

590 vasculature based on tomography of the vessel corrosion casts," Scientific reports, 9(1),
591 pp. 1-11. <https://doi.org/10.6084/m9.figshare.8289869>.
592 [72] Yang, H., Downs, J.C., Girkin, C., Sakata, L., Bellezza, A., Thompson, H., and Burgoyne,
593 C.F., 2007, "3-D histomorphometry of the normal and early glaucomatous monkey optic
594 nerve head: lamina cribrosa and peripapillary scleral position and thickness," Investigative
595 ophthalmology & visual science, 48(10), pp. 4597-4607. [https://doi.org/10.1167/iovs.07-](https://doi.org/10.1167/iovs.07-0349)
596 [0349](https://doi.org/10.1167/iovs.07-0349).
597

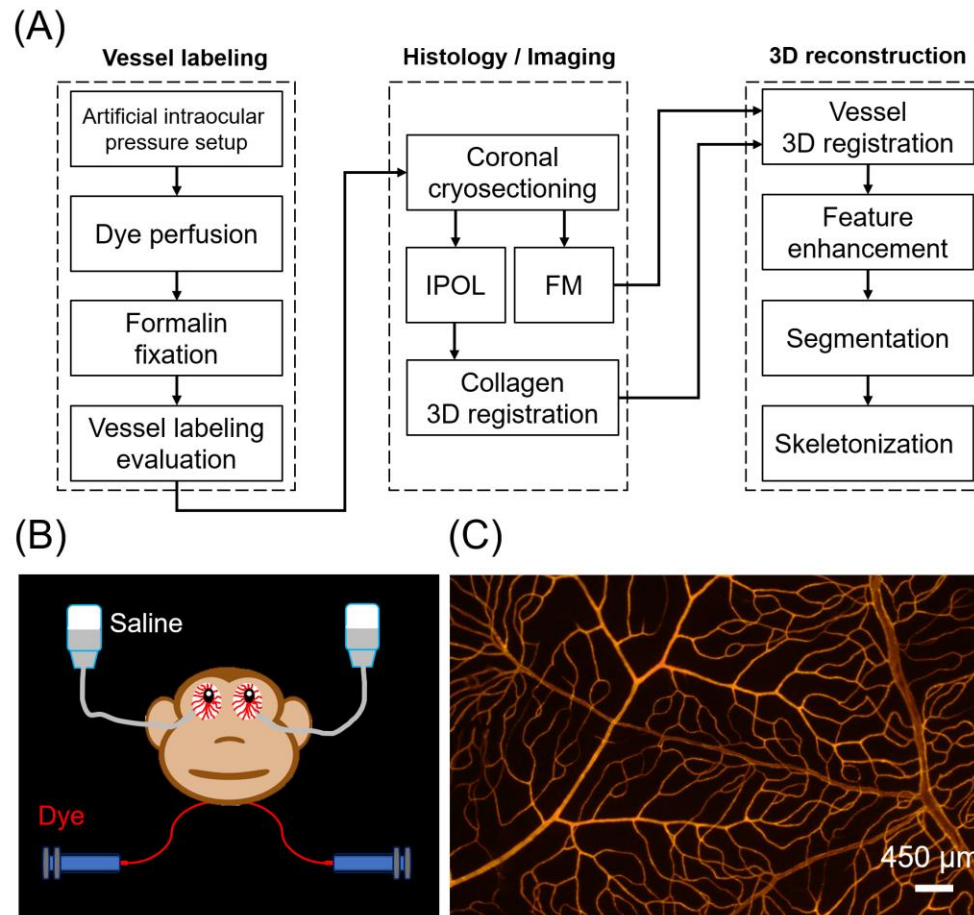


598

599

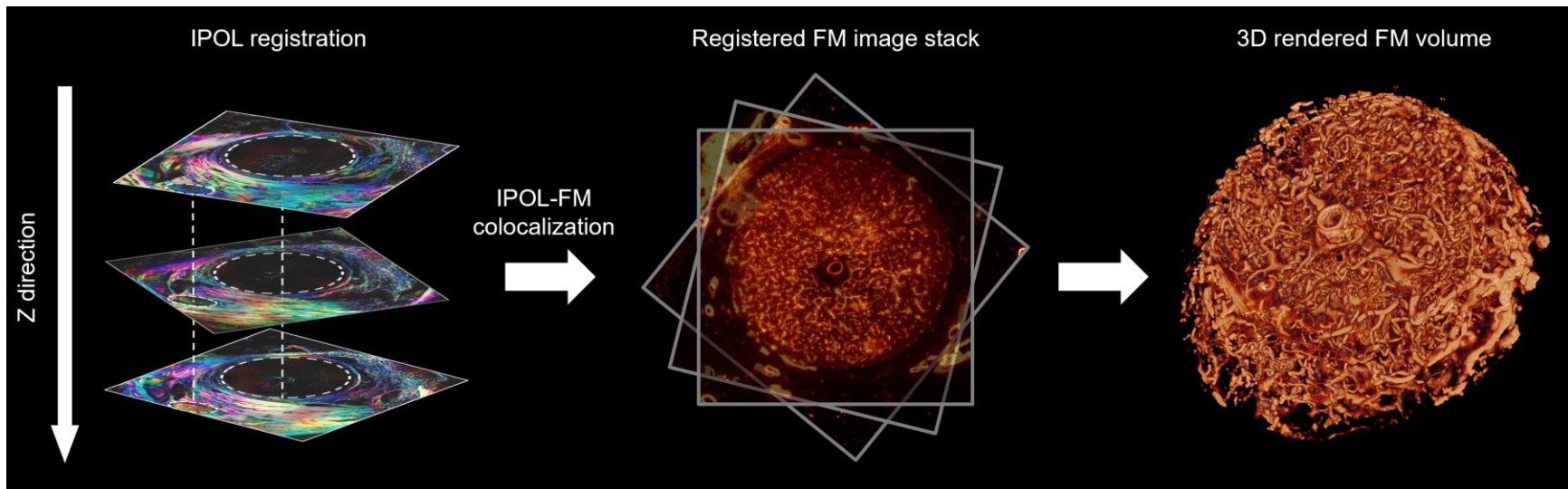
600

Figure 1. Diagram of the eye with defined anterior-posterior direction and coronal plane. Adapted from a diagram by the National Eye Institute.



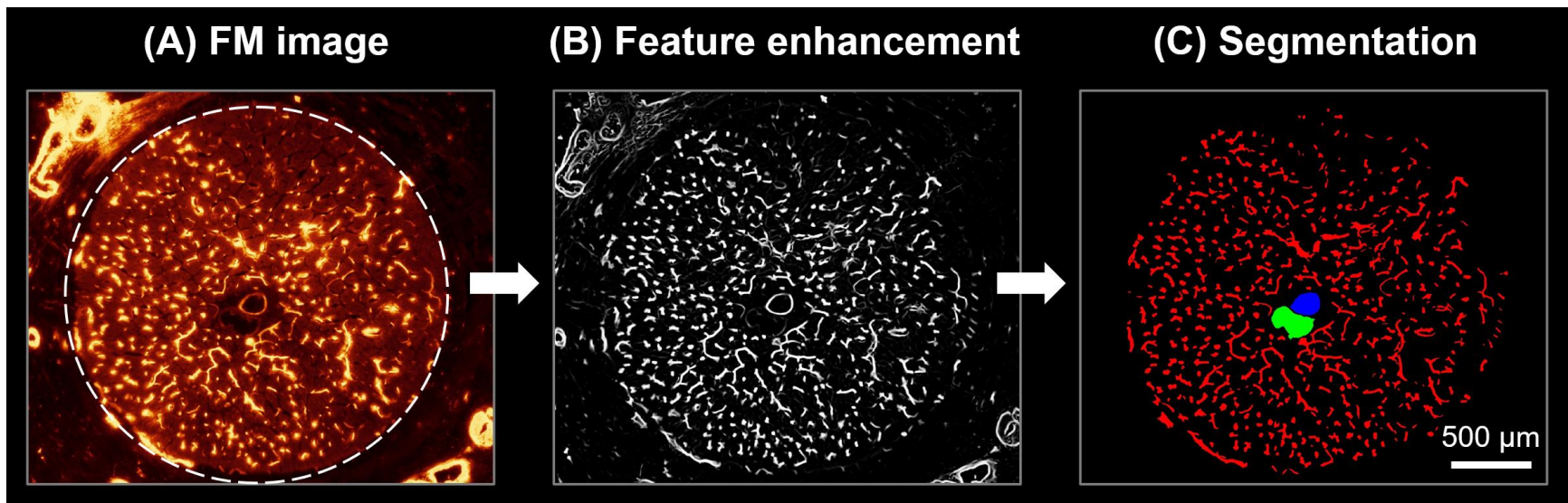
601

602 **Figure 2. (A)** Flow chart of the 3D reconstruction process of an eye-specific vascular network in a monkey ONH (simplified to the key
 603 steps). **(B)** Illustration of the perfusion setup for dye perfusion. Two micro-catheters were inserted into the carotid arteries on each side
 604 of the neck of a monkey for dye perfusion and formalin fixation. A set of isotonic saline columns were used to control the intraocular
 605 pressure of the eyes. **(C)** Example FM image of the vessels in the retina. The image shows continuous staining of the retinal vasculature
 606 without any discernible dark patches or leaks, suggesting the eye had satisfactory posterior pole perfusion, and was therefore candidate
 607 for cryosectioning and reconstruction. A second vessel labeling evaluation was done after the vessel 3D registration to confirm good
 608 quality labeling of ONH vessels (see **Figure 3**).



609

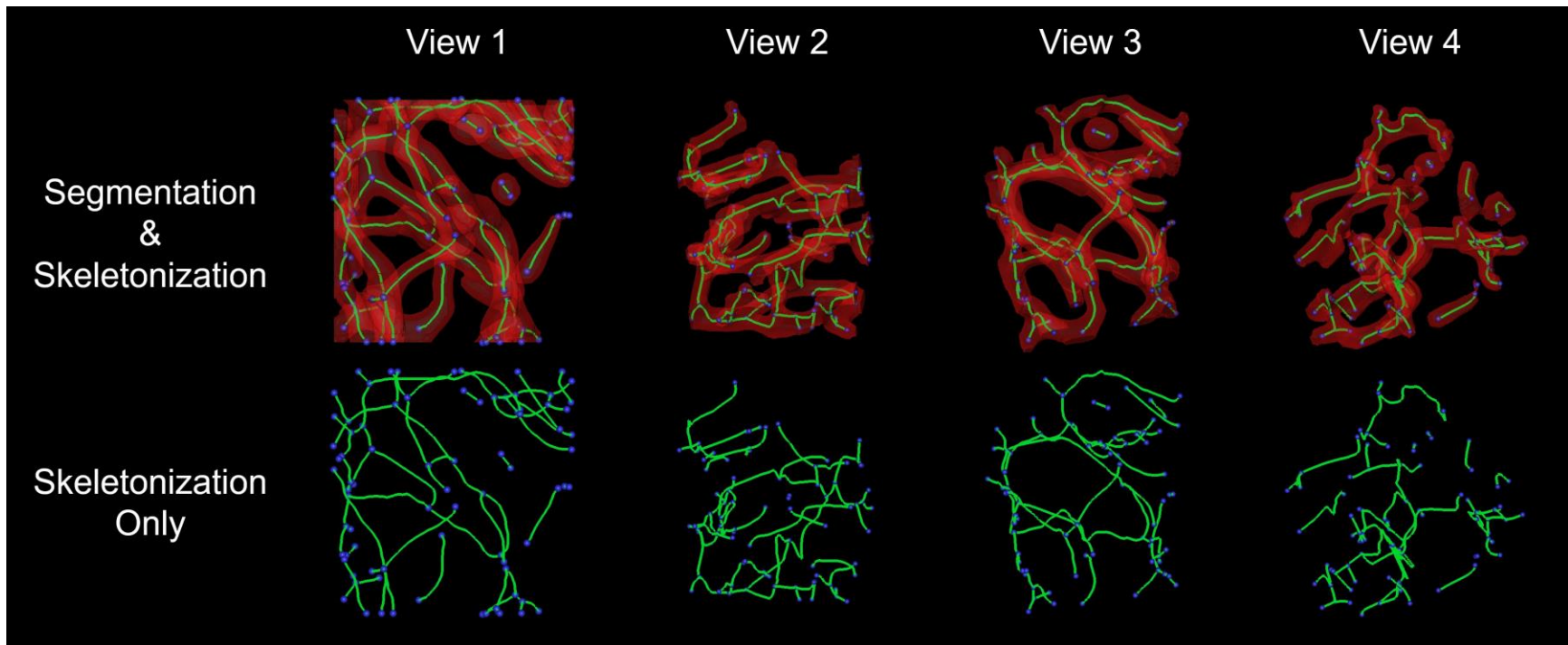
610 **Figure 3.** Illustration of the 3D vessel reconstruction. **Left.** The stack of IPOL images was registered manually based on tissue edges
611 and features (white dashed circles). **Middle.** The transformations (translations and rotation) from IPOL image registration were applied
612 to the stack of FM (vascular) images. **Right:** 3D rendering of the ONH vasculature.



613

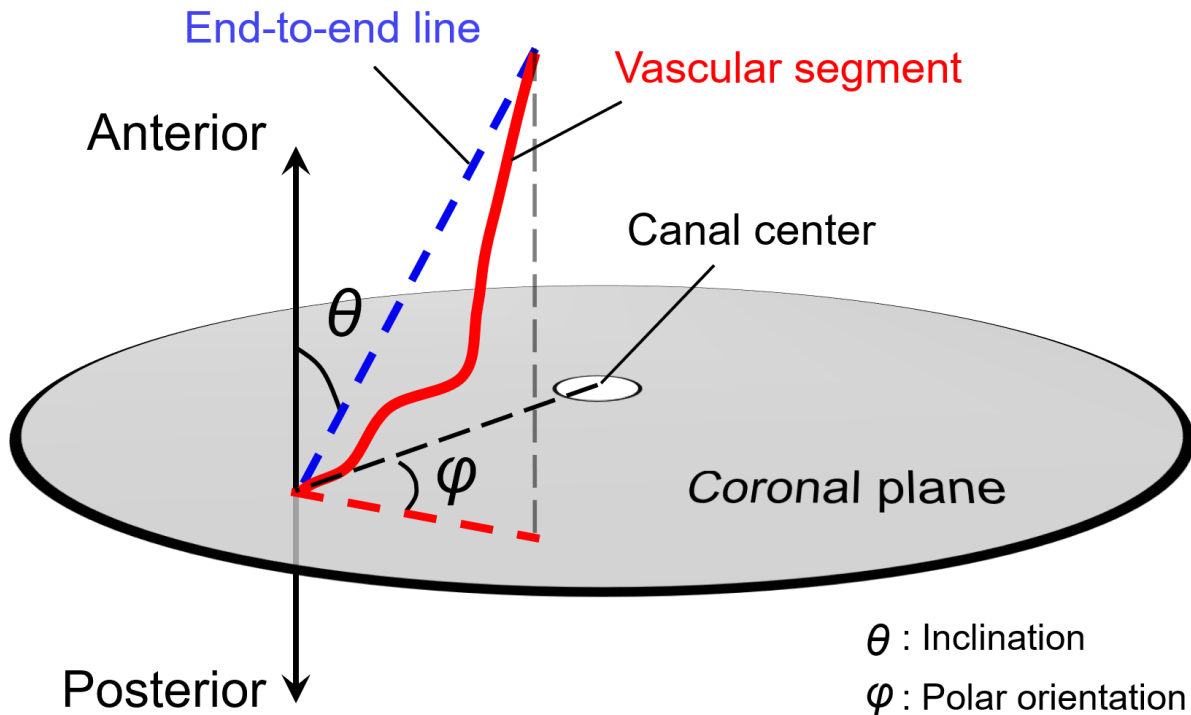
614 **Figure 4.** Vessel segmentation. **(A)** Example FM image of a coronal section through the ONH. Vessels are shown in bright yellow. The
615 white dashed line illustrates the boundary of the scleral canal (exact canal boundaries were obtained from the IPOL images). **(B)** A
616 Frangi filter was used to enhance the vascular features and reduce the background noises on the FM image. **(C)** The feature-enhanced
617 vessels were segmented using the hysteresis thresholding method, and the segmentations were manually checked. We focused on
618 the vessels within the scleral canal. Red – ONH vessels within the canal, Blue – central retinal artery, Green – central retinal vein.

619



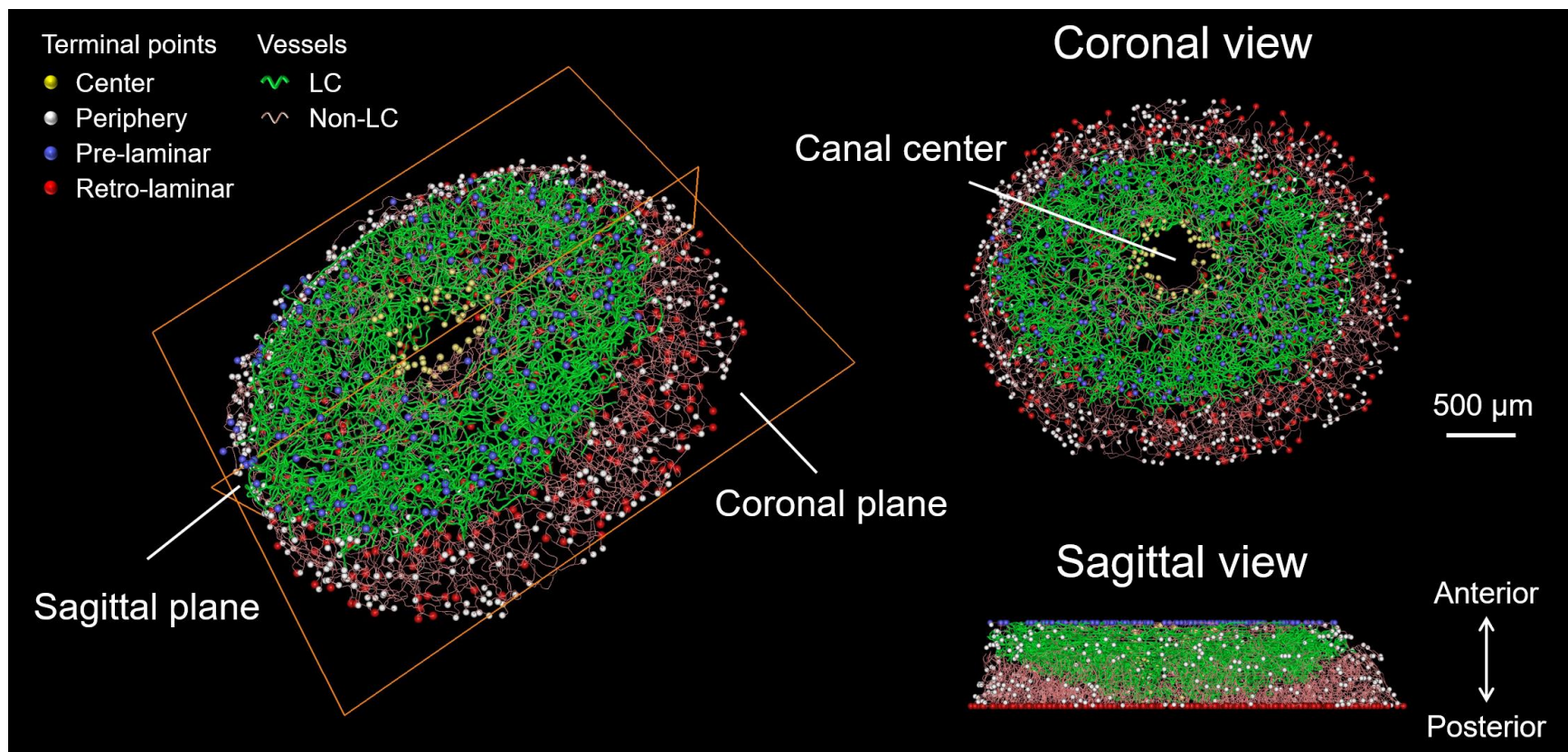
620

621 **Figure 5.** Illustration of vessel skeletonization. We selected a small region of the lamina cribrosa segmentation and skeletonized it.
 622 Shown here are four views of the region. On the top row, the segmentation is shown in semi-transparent red, with green lines and blue
 623 spheres representing skeletonized paths and nodes, respectively. On the bottom row, only the skeletonization is shown. The
 624 skeletonization follows reasonably well the vessel paths without discernible artifacts. The process of selecting a region of the lamina
 625 cribrosa based on flat planes resulted in segments of vessel that did not connect with the rest of the vasculature. These appear as
 626 “islands” in the figure. The vasculature segmentation of the whole lamina had no islands or terminal points within the lamina region.
 627 The islands are useful to illustrate that the skeletonization algorithm dealt fine with discontinuities in the segmentation.



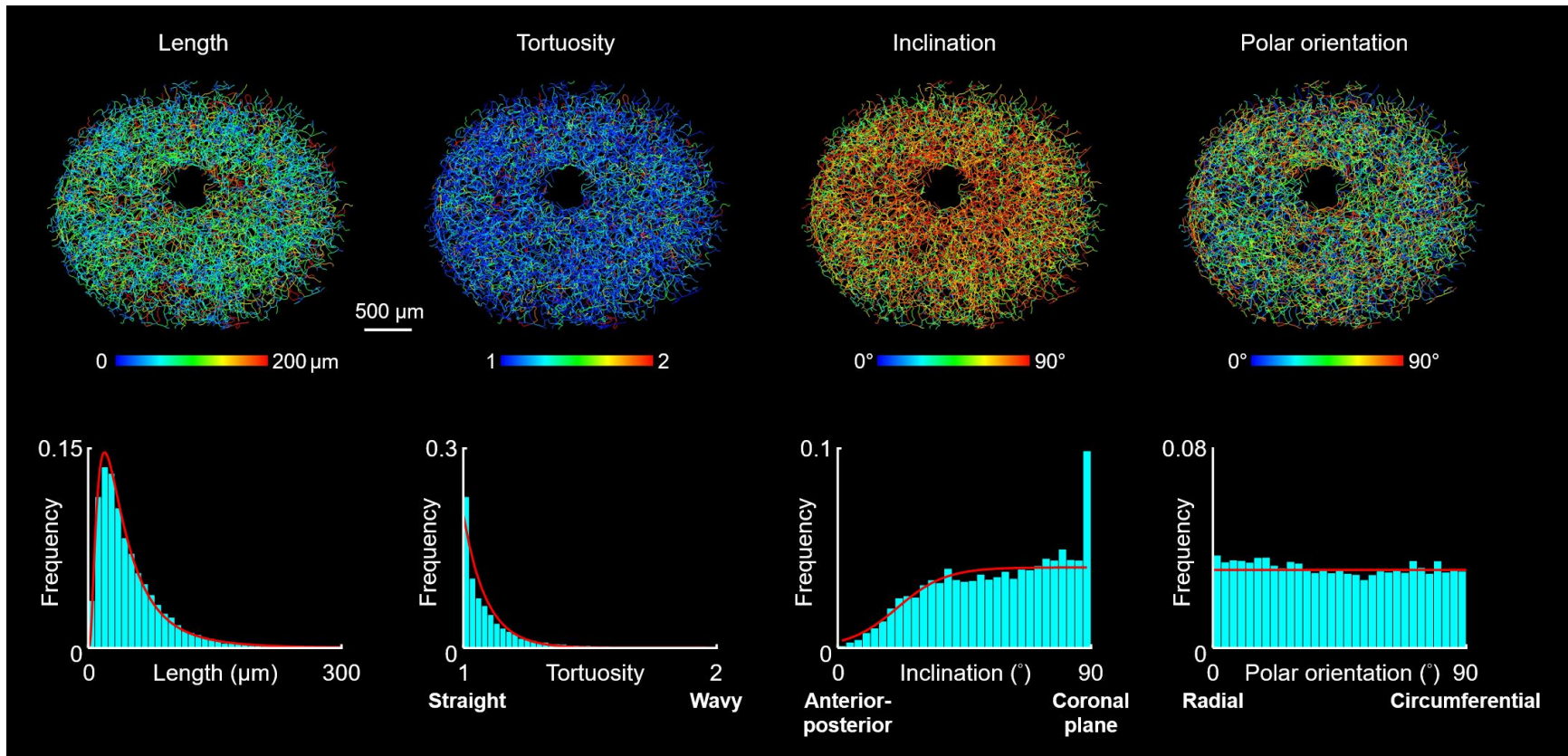
628

629 **Figure 6.** Diagram illustrating the definition of four geometric parameters of a vascular segment:
 630 length, tortuosity, inclination and polar orientation. *Length* was measured as the path length (red
 631 solid line) of the vascular segment. *Tortuosity* (≥ 1) was calculated as the ratio of the path length
 632 to the end-to-end distance (blue dashed line). Tortuosity = 1 indicates that the vessel is straight.
 633 *Inclination* ($0 \leq \theta \leq 90^\circ$) was measured as the angle between the end-to-end line and the anterior-
 634 posterior axis. $\theta=90^\circ$ indicates that the vessel is oriented within the coronal plane. *Polar*
 635 *orientation* ($0 \leq \varphi \leq 90^\circ$) was measured as the angle of the vessel projection on the coronal plane
 636 (red dashed line) relative to the canal center. $\varphi = 0^\circ$ indicates that the vessel is aligned radially
 637 towards/from the canal center, whereas $\varphi = 90^\circ$ indicates that the vessel is aligned
 638 circumferentially.



639

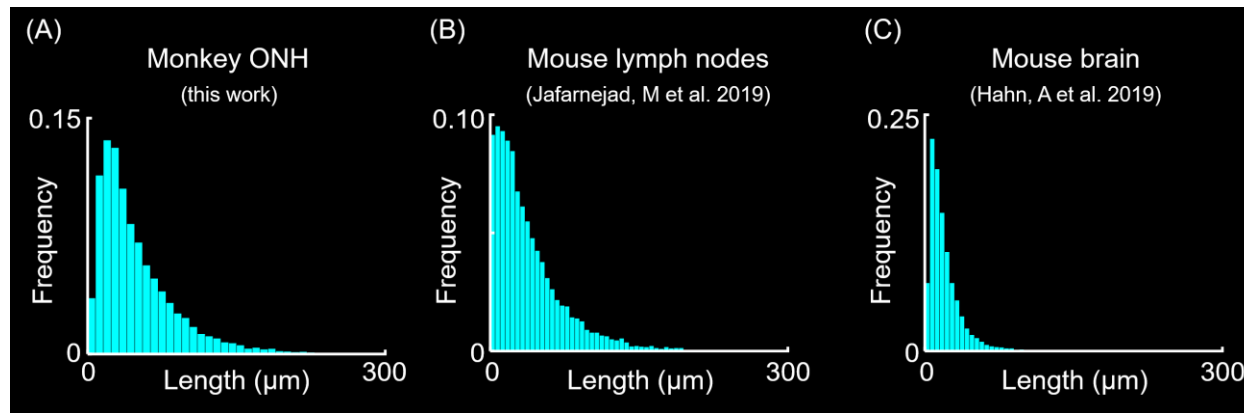
640 **Figure 7.** 3D reconstructed ONH vascular network. The vessels in the lamina cribrosa region are shown thick and colored green, with
 641 the remaining vessels shown thin and colored pink. The entire vascular network consisted of 12,966 vascular segments, 7,989
 642 branching points, and 1,100 terminal points at the network boundaries. The terminal points were colored white at the periphery, yellow
 643 at the center, lavender at the pre-laminar boundary, and red at the retro-laminar boundary, respectively. The gap in the center
 644 corresponds to the locations of the central retinal artery and vein, which were excluded in this study. Note that the 3D view on the left
 645 is perspective without a scale bar, and that the coronal and sagittal views are orthographic and share the same 500-μm scale bar.



646

647 **Figure 8.** Characterization of the four geometric parameters (length, tortuosity, inclination, and polar orientation) of the vessels of the
 648 entire ONH. **Top row:** Vessels of the ONH shown from the front in coronal view colored according to length, tortuosity, inclination, and
 649 polar orientation. The color patterns show that these characteristics were non-uniform throughout the entire network, with no obvious
 650 patterns. **Bottom row:** The distribution of the lengths followed a lognormal distribution (μ [mean of logarithmic values] = 3.6 μm , σ
 651 [standard deviation of logarithmic values] = 0.8 μm), where the mode (*i.e.*, the highest frequency) was calculated as 19.4 μm (about
 652 40% of the average length) and the skewness is 1.9. The distribution of the tortuosities followed an exponential decay (λ [rate parameter]
 653 = 11), where 95% of the vessels had a tortuosity less than 1.46. The frequency of the inclination increased rapidly from 0° to 45°, slowly
 654 thereafter, and spiked at 90°. Polar orientation followed a nearly uniform distribution.

655



656

657 **Figure 9.** Comparison of the vessel length between **(A)** the monkey optic nerve head, **(B)** the mouse lymph nodes [71], and **(C)** the
658 mouse brain [45]. The vessel length consistently followed a lognormal distribution. The vessels in the monkey ONH were longer than
659 in other species and organs. Panels B and C were re-plotted to simplify comparison. **Note the similarity in the distribution shape, despite**
660 **the differences due to tissue and species.**

661

Table 1. Quartiles and functional fits of the vessel geometric parameters.

	25 th percentile	50 th percentile	75 th percentile		Curve fit models	Fitted parameters
Length (μm)	22	38	66	Lognormal	$\frac{1}{x\sigma\sqrt{2\pi}} e^{-\frac{(\ln x - \mu)^2}{2\sigma^2}}$	$\mu = 3.6; \sigma = 0.8$
Tortuosity	1.02	1.06	1.14	Exponential	$\lambda e^{-\lambda(x-x_0)}, x_0=1$	$\lambda = 11$
Inclination ($^\circ$)	39	60	78	Logistic	$\frac{L}{1 + e^{-k(x-x_{50})}}$	$L = 0.04; x_{50} = 21;$ $k = 0.12$
Polar orientation ($^\circ$)	20	43	67	Uniform	$\frac{1}{x_{max} - x_{min}}$	$x_{min} = 0; x_{max} = 90$

663 For reference, the lamina cribrosa is about 3500 μm in diameter, 300 μm in thickness, and about 600 μm from top to bottom (height is
664 larger than thickness because the lamina cribrosa is curved). This means that the median vessel segment is about 1% of lamina
665 cribrosa diameter and 12% of its thickness [72]. Tortuosity varies from 1 for a straight segment to infinity. For comparison, vessels in
666 the porcine ONH have tortuosities from 1 to 1.35 [2]. In terms of the interpretation of the fitted parameters: the logistic model is a
667 function to generate a S-shaped curve, where x_{50} is the x value of the midpoint, k is the steepness of the curve, L is the maximum value
668 of the curve. The parameters x_{min} , x_{max} of the uniform model are values at the extremes of the range.

Table 2. Comparison of the vessel tortuosity in the ONH with other vascular beds.

Tissue	Species	Vessel tortuosity			References
		25 th percentile	50 th percentile	75 th percentile	
ONH	Monkey	1.02	1.06	1.14	Current work
Lamina cribrosa	Pig	1.07	1.17	1.20	[2]
Brain	Mouse	-	1.07	-	[45]
Retina	Human	-	1.08	1.09	[46]
Kidney	Human	1.07-1.08	1.11-1.13	1.15-1.23	[47]
Spleen	Human	1.56	1.73	2.20	[47]